

Article

Effect of the Fluorine Substitution for –OH Group on the Luminescence Property of Eu^{3+} Doped Hydroxyapatite

Xiaojun Zhang, Qingguo Xing, Lixuan Liao and Yingchao Han *

State Key Laboratory of Advanced Technology for Materials Synthesis and Processing, Biomedical Materials and Engineering Research Center of Hubei Province, Wuhan University of Technology, Wuhan 430070, China; zhangxiaojun@whut.edu.cn (X.Z.); xingqingguo_whut@163.com (Q.X.); llx1117@whut.edu.cn (L.L.)

* Correspondence: hanyingchao@whut.edu.cn; Tel: +86-27-87651852; Fax: +86-27-87880734

Received: 6 February 2020; Accepted: 5 March 2020; Published: 10 March 2020



Abstract: In this study, different fluoridated hydroxyapatite doped with Eu^{3+} ion nanoparticles were prepared by the hydrothermal method. The relationship between luminescence enhancement of Eu^{3+} ions and a fluorine substitution ratio for hydroxyl group in hydroxyapatite was discussed. Moreover, the effect of fluorine substitution for a hydroxyl group on phase composition, crystallinity, and crystal size was studied. Phase composition and chemical structures were identified by X-ray diffraction (XRD) and Fourier Transform Infrared (FT-IR) Spectroscopy analyses. Scanning Electron Microscopy (SEM) and Transmission Electron Microscopy (TEM) patterns were performed to analyze the morphology and particle size. X-ray Photoelectron Spectroscopy (XPS) patterns were observed to analyze fluorine substitution for the hydroxyl group and chemical state of Eu^{3+} ions in fluoridated hydroxyapatite. The results of these experiments indicated that the samples with a different fluorine substitution ratio were prepared successfully by maintaining the apatite structure. With an increasing fluorine substitution ratio, the morphology maintained a rod-like structure but the aspect ratio tended to decrease. XPS patterns displayed that the fluorine replaced the hydroxyl group and brought environmental variation. The fluorine ions could affect the crystal field environment and promote luminescence conversion. There was a linear relationship between the fluorine substitution ratio and luminescence enhancement.

Keywords: $\text{Eu:F}_x\text{H}_{1-x}\text{Ap}$ nanoparticles apatite; europium; luminescence

1. Introduction

Hydroxyapatite ($\text{Ca}_{10}(\text{PO}_4)_6(\text{OH})_2$), which is also known as HAp, is the main inorganic ingredient of hard tissues similar to its mineral constituents [1–3], which have outstanding biocompatibility and bioactivity [4,5]. Meanwhile, HAp crystals are good host material for doping of rare earth (RE) ions, and the doped HAp such as Eu:HAp [3], Eu/Tb:HAp [6], and Eu/Dy:HAp [1] display unique luminescence properties under excitation of a specific wavelength. Moreover, the RE ions doped HAp nanoparticles have better features as luminescence imaging agents including low toxicity, photostability, thermal and chemical stability, and real-time imaging [4,7–9]. Their luminescence imaging ability is affected by a degree of crystallinity, size distribution, and dispersion of nanoparticles as well as crystal field contributions [1,5,10].

Recently, more attention has been put by the researchers toward the luminescence performance of RE ions in natural as well as synthesized apatites. The main focus for the study of RE ions doped with HAp has been the enhancement of luminescence with previous results showing the possibility of improving luminescence performance of RE elements doped HAp by increasing the RE content [11], calcination [3], and co-doping of RE ions [12–14]. However, they are accompanied by certain issues like quenching effect, oversize, severe aggregation, and toxicity. Fluoride ions (F^-) are usually used for

replacing the hydroxyl (–OH) group of HAp to improve some physicochemical properties such as solubility, crystallinity, and resistance to acid corrosion [15]. Moreover, the Eu^{3+} ions in fluorapatite ($\text{Ca}_{10}(\text{PO}_4)_6\text{F}_2$, FAp) emits stronger luminescence than that in HAp, which can be attributed to the effect of F^- ions on the crystal field environment. The –OH group in the crystal lattice has a quenching effect on luminescence of rare earth ions. The F^- ions can generate lower vibration energy and, thereby, promote luminescence conversion [16]. However, the relationship between the fluorine substitution ratio for the –OH group and luminescence of Eu^{3+} ions has not been revealed in detail.

Herein, we used a hydrothermal synthetic route to prepare fluoridated hydroxyapatite doped with Eu^{3+} ions ($(\text{Ca}, \text{Eu})_5(\text{PO}_4)_3(\text{OH})_{1-x}\text{F}_x$, $\text{Eu:F}_x\text{H}_{1-x}\text{Ap}$). The change of luminescence was observed with varying fluorine substitution ratio (from 0 to 1) for the –OH group, which aims to reveal the relationship between the fluorine substitution ratio and luminescence intensity. Moreover, the effect of the fluorine substitution ratio for the –OH group on phase composition, crystallinity, crystal size, and chemical state of Eu^{3+} was studied by X-ray diffraction (XRD), Fourier Transform Infrared (FT-IR) Spectroscopy, Scanning Electron Microscopy (SEM), High Resolution Transmission Electron Microscope (HRTEM), Energy Dispersive Spectrometer (EDS), and X-ray Photoelectron Spectroscopy (XPS).

2. Materials and Methods

2.1. Preparation of $\text{Eu:F}_x\text{H}_{1-x}\text{Ap}$ Nanoparticles

The nanocrystalline $\text{Eu:F}_x\text{H}_{1-x}\text{Ap}$ materials were obtained using the following hydrothermal method. First, $\text{CaCl}_2 \cdot 2\text{H}_2\text{O}$, $\text{Na}_2\text{HPO}_4 \cdot 12\text{H}_2\text{O}$, $\text{Eu}(\text{NO}_3)_3 \cdot 6\text{H}_2\text{O}$, and NaF were dispersed individually in deionized water. Na_2HPO_4 and NaF powders were dissolved in deionized water to get solution A (PO_4^{3-} : 0.24 mol/L, F^- : 0.08x mol/L). $\text{CaCl}_2 \cdot 2\text{H}_2\text{O}$ and $\text{Eu}(\text{NO}_3)_3 \cdot 6\text{H}_2\text{O}$ powders were dissolved in deionized water to get solution B (Ca^{2+} : 0.393 mol/L, Eu^{3+} : 0.008 mol/L). Second, 15 ml of solution A was poured into 15 ml of solution B under vigorous stirring to get the suspension. The pH value of the suspension was adjusted to about 9.0–9.5 by NH_3 solution. Subsequently, the suspension was moved to a sealed stainless-steel autoclave, and maintained at a stirring condition at 120 °C for 60 min. After being naturally cooled at room temperature, the resulting milky matter was separated by centrifugation at 2000 rpm for 5 min, and washed three times using deionized water. Lastly, it was freeze dried for 20 hours to get the powder sample. The molar ratios of $(\text{Ca} + \text{Eu})/\text{P}$ and $\text{Eu}/(\text{Ca} + \text{Eu})$ were 1.67 and 0.02, respectively. The amount of F^- was adjusted to obtain a different fluorine substitution ratio for the –OH group depending on the x value in $\text{Eu:F}_x\text{H}_{1-x}\text{Ap}$ (x = 0, 0.1, 0.3, 0.5, 0.7, 0.8, and 1).

2.2. Characterization of $\text{Eu:F}_x\text{H}_{1-x}\text{Ap}$ Nanoparticles

The phase composition, crystalline structure, and the crystallinity of the $\text{Eu:F}_x\text{H}_{1-x}\text{Ap}$ were explored by XRD (D/Max-III A, Rigaku Co., Tokyo, Japan). The 2θ range of the XRD pattern was collected from 10° to 70° with a scanning speed of 0.02°/s.

The degree of crystallinity X_c for $\text{Eu:F}_x\text{H}_{1-x}\text{Ap}$ was calculated by the following equation.

$$X_c = \left[1 - \frac{v_{112/300}}{I_{300}} \right] \quad (1)$$

where $v_{112/300}$ is the hollow intensity between the planes (112) and (300) reflection, and I_{300} is the intensity of the plane (300) diffraction peak [1,17]. Moreover, crystallite sizes D of Eu: HAp were concluded by using Scherer's Equation.

$$D = \frac{K \cdot \lambda}{\text{FWHM}_{002} \cdot \cos \theta} \quad (2)$$

where the shape factor K is 0.9, wavelength λ is 0.15418, FWHM_{002} express the full width at half maximum for reflection of the plane (002), and θ stands for the angle of a certain signal [1,3,18]. FT-IR (Nexus, Thermo Nicolet, USA) was exploited to analyze the material's vibrational modes of the characteristic band.

The spectra were recorded between 4000 cm^{-1} to 400 cm^{-1} . The $\text{Eu:F}_x\text{H}_{1-x}\text{Ap}$ powders (7.5 mg) were dispersed in alcohol (5 ml) and then the suspension was acquired by ultrasonic cleaning. The morphology and the average particle size of $\text{Eu:F}_x\text{H}_{1-x}\text{Ap}$ were evaluated by SEM (JSM-5610LV, JEOL, Japan) and HRTEM (JEM-2100 F, JEOL, Japan). XPS (ESCALAB 250Xi/ESCALAB 250Xi) was used to identify the composition and chemical states of the elements. The luminescence spectra of $\text{Eu:F}_x\text{H}_{1-x}\text{Ap}$ was recorded using a 970CRT Luminescence Spectrophotometer (Shanghai Sanco, China). An emission spectrum (or excitation spectrum) was recorded by fastening the excitation wavelength (or emission wavelength) while scanning the determined wavelength region of the spectrofluorimeter [19].

The luminescence enhancement relative ratio (R) was calculated by the following equation.

$$R = \frac{B - A}{A} \cdot 100\% \quad (3)$$

where A is the emission peak's intensity of Eu:HAp and B is the emission peak's intensity of $\text{Eu:F}_x\text{H}_{1-x}\text{Ap}$.

The luminescence lifetime and quantum yield were measured by FLS980 Series of Fluorescence Spectrometers. The average luminescence lifetime ($\tau_{(\text{avg})}$) was calculated by the following equation.

$$\tau_{(\text{avg})} = \frac{A_1\tau_1^2 + A_2\tau_2^2}{A_1\tau_1 + A_2\tau_2} \quad (4)$$

where A_1 and A_2 are the exponential factors. τ_1 and τ_2 are luminescence lifetime values of $\text{Eu:F}_x\text{H}_{1-x}\text{Ap}$.

3. Results

3.1. Phase Composition and Chemical Structure

Figure 1A shows the phase composition. Crystallite crystal and the degree of crystallinity of samples have different fluorine substitution ratios. By comparing the XRD patterns, it was observed that no additional diffraction peaks appeared in the case of $\text{Eu:F}_x\text{H}_{1-x}\text{Ap}$ nanoparticles except for characteristic diffraction peaks of FAp (PDF # 75-0915) and HAp (PDF # 74-0566), which indicates no impurity phase. Moreover, with the gradual increase of a fluorine substitution ratio, the diffraction angle and relative intensity varied slightly. Considering that the F^- ions (1.28 \AA) are smaller than the $-\text{OH}$ group (1.37 \AA), with an increasing fluorine substitution ratio, there would be natural shrinkage of the lattice leading to a slight shift of the diffraction signals to higher degrees. The calculated crystallite sizes assigned to (002) diffraction peaks with a different fluorine substitution ratio, respectively, also indicated that the crystallite sizes tended to reduce (Table A1). Moreover, the crystallinity also decreased with the increase of the fluorine substitution ratio from 0 to 0.5. When the fluorine substitution ratio was above 0.5, the crystallinity gradually grew with an increasing substitution content (Table A1). In addition, the crystallinity of Eu:FAP was as high as 55.56%, which was higher than the crystallinity of Eu:HAp (38.73%).

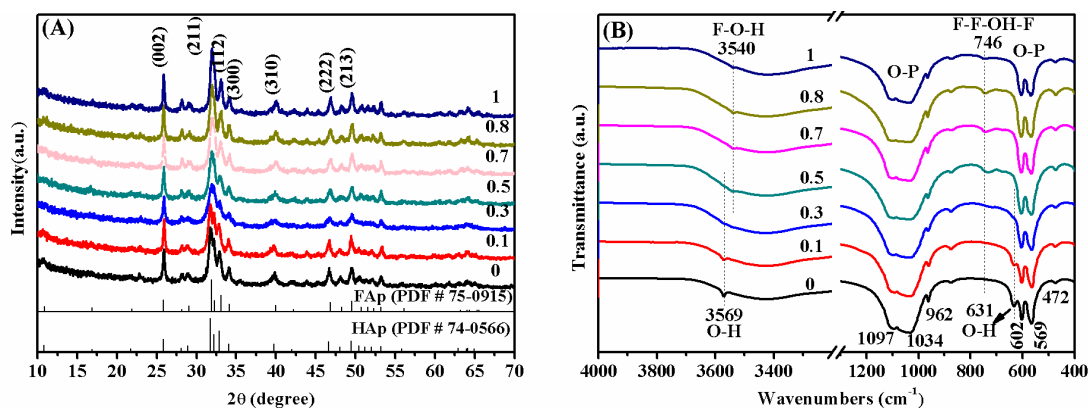


Figure 1. Cont.

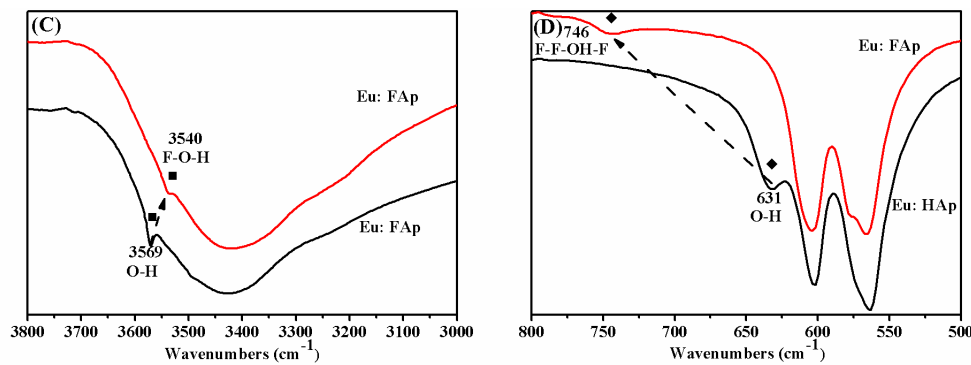


Figure 1. (A) XRD patterns and (B) FT-IR spectra of the $\text{Eu:F}_x\text{H}_{1-x}\text{Ap}$ ($x = 0, 0.1, 0.3, 0.5, 0.7, 0.8, 1.0$) powders with a different fluorine substitution ratio (C) and (D) corresponding to the conversion of Eu:HAp and Eu:FAP absorption peaks.

Figure 1B shows FT-IR spectra of $\text{Eu:F}_x\text{H}_{1-x}\text{Ap}$ samples. In the FT-IR spectrum of Eu:HAp samples without F^- ions substitution, the vibrational peaks of PO_4^{3-} group in the apatite structure was distinguished, including ν_1 (at 962 cm^{-1}), ν_2 (at 472 cm^{-1}), ν_3 (at 1034 cm^{-1} and 1107 cm^{-1}), and ν_4 (at 564 cm^{-1} and 602 cm^{-1}) [20,21]. Hydroxyapatite is a kind of apatite crystal whose general molecular formula is $\text{Me}_{10}(\text{XO}_4)_6\text{Y}_2$. In this study, the Me is a divalent cation, XO_4 is the negative trivalent group, and Y is a negative monovalent ion [22]. For RE-doped apatite with a different fluorine substitution ratio, RE ions will occupy the position of Me and Y will be replaced by F^- ions. Accordingly, the position and the intensity of the vibrational peak of the $-\text{OH}$ group in the spectrum changes with the fluorine substitution ratio. When the F^- ions enter into the lattice of HAp, the original H-O-H is gradually converted into the F-O-H structure, which is attributed to the hydrogen bond formed by the F^- ions (Figure 1C). This will generate a new chemical bond accompanied by a new vibration mode (F-O-H) and causes the decrease of the H-O-H vibration [23]. Due to higher electronegativity of F^- ions compared to O^{2-} ions, a new vibration (F-F-OH-F) will also be detected at about 746 cm^{-1} (Figure 1D). Results showed that the absorption peaks of the $-\text{OH}$ group was decreased at 3569 cm^{-1} and 631 cm^{-1} with an increase of the fluorine substitution ratio. The absorption peaks at 3540 cm^{-1} (F-O-H) and 746 cm^{-1} (F-F-OH-F) appeared and the intensity was enhanced. This indicated that the F^- ions replaced the $-\text{OH}$ group and entered into the apatite crystal lattice in the case of $\text{Eu:F}_x\text{H}_{1-x}\text{Ap}$ samples. The hygroscopic property is related to the surface chemical property [24]. For example, the $-\text{OH}$ group makes it easy to form hydrogen bonds with water molecules, which make the water molecules absorb on the surface of materials. This is conducive toward improving the hygroscopic property [24,25]. The chemical property of the apatite surface was changed when the $-\text{OH}$ group was replaced by F^- ions. The $-\text{OH}$ group on the surface of HAp easily forms hydrogen bonds with water and absorbs on the surface of HAp. Therefore, HAp has a certain hygroscopic property. After replacing the $-\text{OH}$ group, the hygroscopic property exhibited by hydrogen bonding is weakened. Therefore, the hygroscopic property is reduced after F^- ions replace the $-\text{OH}$ group.

3.2. Morphology Observation

Figure A1 shows the SEM images of as-dried $\text{Eu:F}_x\text{H}_{1-x}\text{Ap}$ powders with a different fluorine substitution ratio. The morphology was mainly rod-like, and the length of the rod-like particles tended to decrease with the increase of the fluorine substitution ratio. The EDS spectrum further showed the signals of Ca, Eu, O, P, and F in $\text{Eu:F}_x\text{H}_{1-x}\text{Ap}$ ($x = 1$) (Figure A2). The calculated molar ratios of $\text{Eu}/(\text{Ca} + \text{Eu})$, $(\text{Ca} + \text{Eu})/\text{P}$, and $\text{F}/(\text{Ca} + \text{Eu})$ were 0.02 ± 0.01 , 1.69 ± 0.05 , and 0.24 ± 0.04 , respectively, which were consistent with the setting values (Table A2).

TEM observations showed that samples consisted of short rod-like nanoparticles (Figure 2). The average length and diameter of the nanoparticles were obtained by collecting data of more than 100 particles (Table A3). With the increase of the fluorine substitution ratio from 0 to 1, the length of

the particles was decreased significantly from 77.7 ± 2.9 nm to 43.4 ± 2.0 nm. However, the diameter of the particles varied little (between 15.4 nm and 14.1 nm). This led to the decrease of the aspect ratio of rod-like particles from about 5 to about 3. Furthermore, the lattice planes of (002), (300) were observed in the HRTEM images (Figure 2), which were assigned to an apatite crystal structure. With the increase of the fluorine substitution ratio, the interfacial spacing of (002) decreased slightly, which was consistent with the change of length of rod-like particles. In addition, the capillary phenomenon between particles will make the water molecules absorbed on the particles [26]. However, the capillary and mesoporous structures were not observed in the microstructure of the $\text{Eu:F}_x\text{H}_{1-x}\text{Ap}$ synthesized by the hydrothermal method. Therefore, the hygroscopic property was not improved with fluorine substitution.

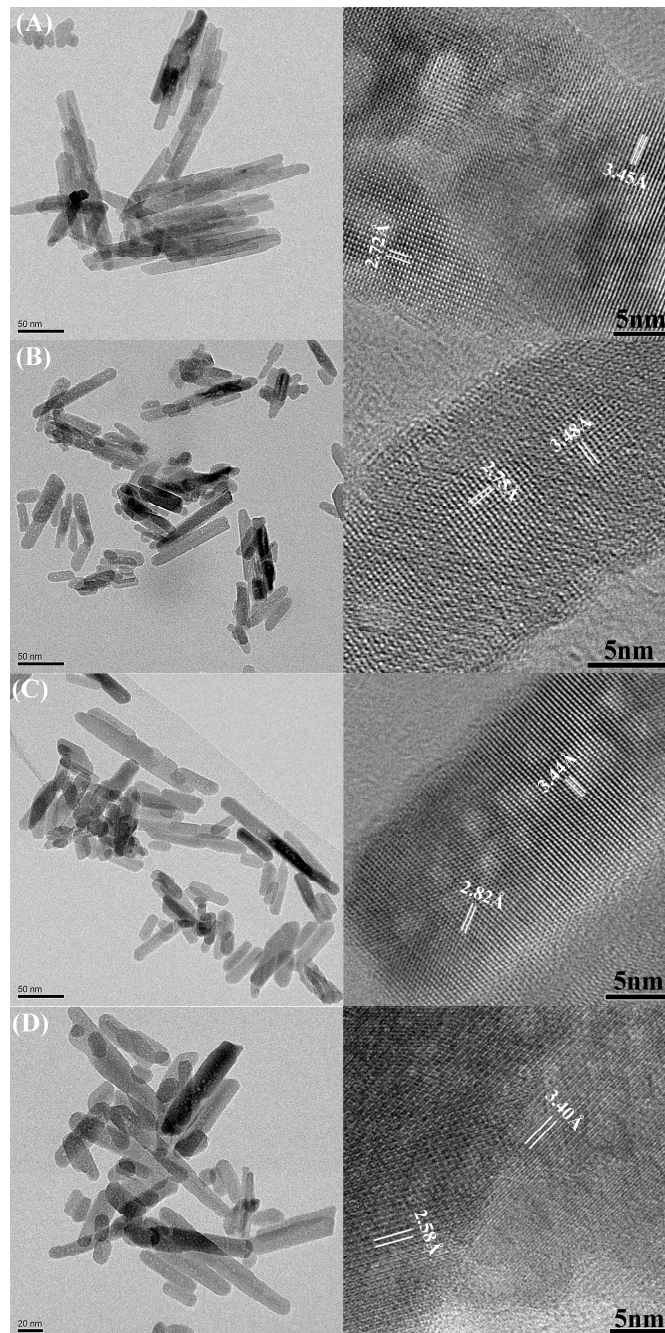


Figure 2. TEM images of $\text{Eu:F}_x\text{H}_{1-x}\text{Ap}$ prepared by the hydrothermal method. (A): $x = 0$, (B): $x = 0.3$, (C): $x = 0.5$, (D): $x = 1$.

3.3. XPS

Figure 3A shows the XPS spectra of $\text{Eu:F}_x\text{H}_{1-x}\text{Ap}$ ($x = 0, 0.3, 0.5, 0.8,$ and 1) samples. For the samples, the characteristic peaks of Ca 2p, P 2p, O 1s, and Eu 3d were all detected. Moreover, with the increase of the fluorine substitution ratio, the characteristic peak of F 1s was enhanced gradually, which indicates that the F^- ions entered into the apatite lattice (Figure 3B) [27]. When the F^- ions entered into the apatite lattice, the binding energy of the atom varied due to the change in chemical environments, corresponding to a shift of the peak position in the XPS spectrum. For example, the binding energy of Eu^{3+} increased from 1134.73 eV to 1135.33 eV while the x increased from 0 to 1. This indicated that the surrounding environment for Eu^{3+} ions was changed due to the fluorine substitution for the $-\text{OH}$ group.

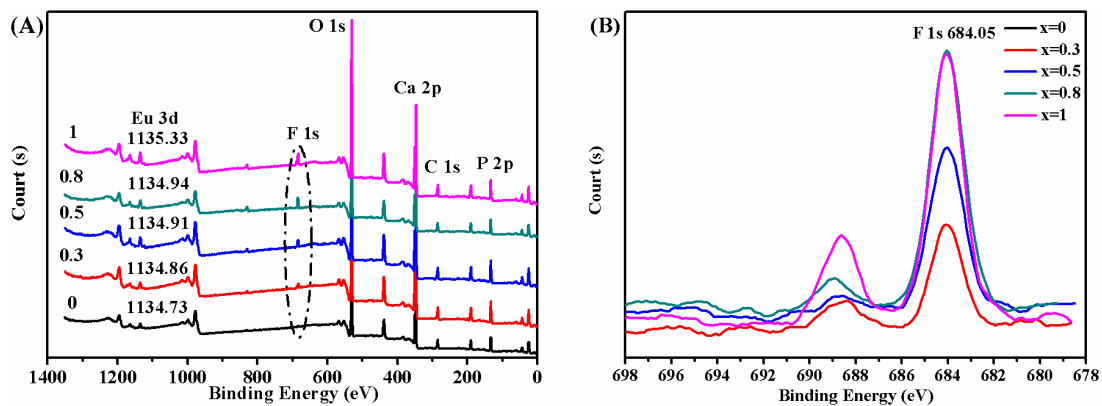


Figure 3. The XPS spectra of $\text{Eu:F}_x\text{H}_{1-x}\text{Ap}$ ($x = 0, 0.3, 0.5, 0.8$ and 1) (A) Survey scan spectrum. (B) High-resolution scan spectra of F 1s.

3.4. Luminescence Spectrum

The luminescence property of $\text{Eu:F}_x\text{H}_{1-x}\text{Ap}$ with a different fluorine substitution ratio was detected. Figure 4 shows the excitation spectra with the emission at 617 nm. Results showed the strongest peak at 394 nm and some smaller peaks at 364 nm, 381 nm, and 264 nm, respectively. The smaller peak at 264 nm derived from the Eu-O bonds belong to a process of energy transfer. The peaks at 394 nm, 364 nm, and 381 nm were due to the electric dipole forbidden intra-configurational f-f transitions [28]. Furthermore, with the increase of the fluorine substitution ratio, the intensity of excitation peaks was enhanced gradually.

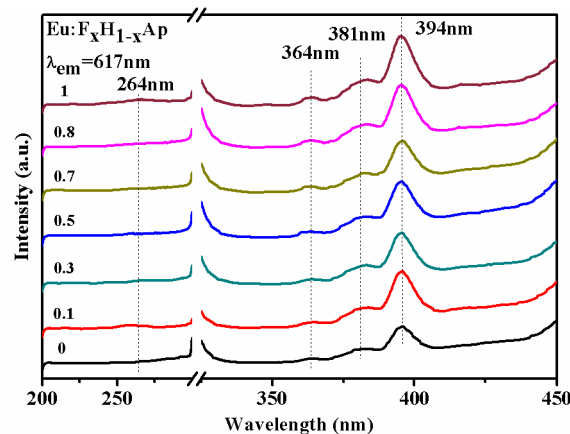


Figure 4. Luminescence excitation spectra of $\text{Eu:F}_x\text{H}_{1-x}\text{Ap}$ ($x = 0, 0.1, 0.3, 0.5, 0.7, 0.8, 1.0$) emission at 617 nm.

With the excitation at 394 nm (Figure 5A), the emission spectra display the strongest peak at 617 nm ($^5D_0 \rightarrow ^7F_2$) and three smaller peaks at 594 nm ($^5D_0 \rightarrow ^7F_1$), 654 nm ($^5D_0 \rightarrow ^7F_3$), and 699 nm ($^5D_0 \rightarrow ^7F_4$). The luminescence signal at 617 nm was stronger than that at 590 nm. In the hydroxyapatite structure, two Ca sites can be occupied by Eu^{3+} ions. One is Ca (I) with C_3 symmetry surrounded by 9 oxygens. The other is Ca (II) with Cs symmetry surrounded by six oxygens and one $-\text{OH}$ group [9,29]. Eu^{3+} ions located in Ca (I) site show the main emission at about 618 nm, and the main emission appears at about 573–578 nm for Eu^{3+} ions in Ca (II) site [29]. Therefore, in our study, the Eu^{3+} ions predominantly occupied the Ca (I) site (C_3 symmetry) in $\text{Eu:F}_x\text{H}_{1-x}\text{Ap}$ [30]. The luminescence intensity enhanced with the increase of the fluorine substitution ratio and the peak at 617 nm increased significantly. The luminescence enhancement relative ratio was further calculated using the emission peak at 617 nm (Figure 5B). Results displayed that the luminescence enhancement showed a near linearly increasing relationship with the increase of a fluorine substitution ratio. Under excitation at 264 nm and 394 nm, the emission peaks of $\text{Eu:F}_x\text{H}_{1-x}\text{Ap}$ nanoparticles were observed at 594 nm, 617 nm, 654 nm, and 699 nm ranging from 550 nm to 750 nm, where the transitions of Eu^{3+} ions were $^5D_0 \rightarrow ^7F_1$, $^5D_0 \rightarrow ^7F_1$, $^5D_0 \rightarrow ^7F_3$ and $^5D_0 \rightarrow ^7F_4$, respectively. The luminous mechanism may be explained by the energy level diagram (Figure 6). With the increase of a fluorine substitution ratio, the emission peak position of $\text{Eu:F}_x\text{H}_{1-x}\text{Ap}$ in luminescence spectra was not moved and the peak intensity was gradually enhanced. Especially, the relationship between the luminescence enhancement and fluorine substitution ratio displayed a nearly linear relationship. Accordingly, it can be expected that the fluorine content in $\text{Eu:F}_x\text{H}_{1-x}\text{Ap}$ can be estimated by determining the luminescence of Eu^{3+} ions.

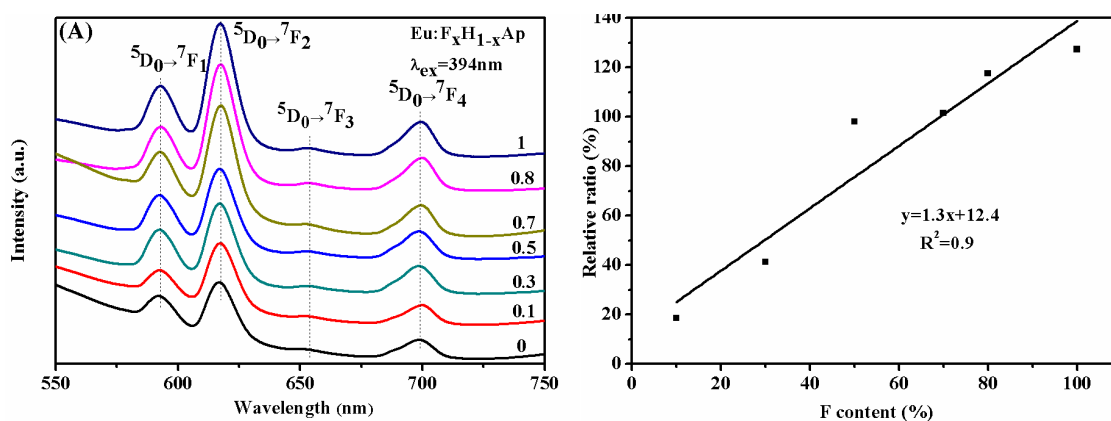


Figure 5. (A) Luminescence spectra of $\text{Eu:F}_x\text{H}_{1-x}\text{Ap}$ ($x = 0, 0.1, 0.3, 0.5, 0.7, 0.8, 1.0$) excitation at 394 nm and (B) the relative ratio with a different fluorine ratio.

The emissions of Eu^{3+} excited at 394 nm could be attributed to the two transition modes including electric dipole transition (ED transition) and a magnetic dipole transition (MD transition) [19,31]. The majority of them belonged to ED transition, and some transitions such as the $^5D_0 \rightarrow ^7F_1$ transition belonged to the MD transition. The $^5D_0 \rightarrow ^7F_2$ transition was greatly affected by the surrounding symmetry of the Eu^{3+} ions and properties of the host materials, which was much stronger than the other ED transition. This is also called “hypersensitive transition” [19,32,33]. The $^5D_0 \rightarrow ^7F_1$ MD transition is largely independent of the environment of the Eu^{3+} ions and its intensity is often used as a calibration for comparing luminescence spectra [19]. Furthermore, the transition intensity ratio of $^5D_0 \rightarrow ^7F_2$ (I_R) to $^5D_0 \rightarrow ^7F_1$ (I_0) was calculated to reveal the change of the environment of Eu^{3+} ions. Results showed that the value of I_R/I_0 was increased with the increase of fluorine substitution ratio, which indicates that the surrounding environment of Eu^{3+} ions became more asymmetric. It could be inferred that the fluorine substitution for the $-\text{OH}$ group changed the environment of Eu^{3+} ions and caused the rise of asymmetry. In addition, the fluorine ions have lower vibrational energy than the $-\text{OH}$ group. This will be favorable for Eu^{3+} ions’ luminescence transition [5]. Therefore, in the matrix of apatite, the fluorine

substitution for the –OH group could decrease the luminescence quenching of Eu^{3+} ions, which is caused by the –OH group and promotes the luminescence conversion.

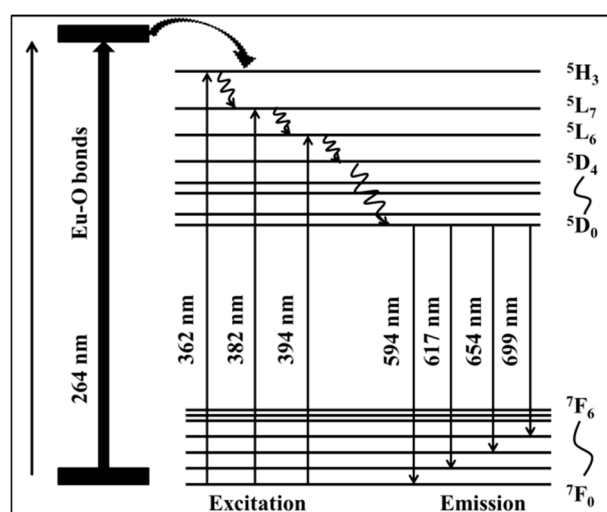


Figure 6. Energy level diagram for a luminous mechanism of $\text{Eu:F}_x\text{H}_{1-x}\text{Ap}$.

Figure 7 shows the decay curves of Eu:HAp and Eu:FAp . Under 394-nm excitation, the average luminescence lifetime of Eu:HAp and Eu:FAp were $727 \mu\text{s}$ and $1016 \mu\text{s}$. The absolute quantum yield of Eu:HAp and Eu:FAp were 1.51% and 8.96%, respectively. The results showed that the luminescence lifetime and quantum yield increased when the –OH group was replaced by F^- ions.

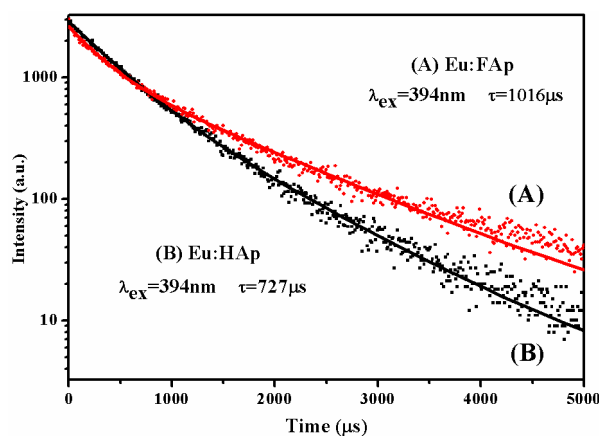


Figure 7. Decay curves monitored at 617 nm of (A) $\text{Eu}^{3+}:\text{HAp}$ and (B) $\text{Eu}^{3+}:\text{FAp}$.

With the excitation at 264 nm (Figure 8A), the emission spectra display four peaks similar to those excited at 394 nm (594 nm, 617 nm, 654 nm, and 699 nm). With the increase of the fluorine substitution ratio, the luminescence intensity was gradually enhanced. For example, the luminescence enhancement of peak at 617 nm increased significantly (Figure 8B). In addition, the relative ratio also showed a nearly linear increasing relationship with the increase of the fluorine substitution ratio. The emission peaks were determined by the charge transfer of the Eu-O bond, which is also called the charge transfer band (CTB) (Figure 6) [19,26]. The O^{2-} ions absorb energy and transfer to Eu^{3+} ions through the Eu-O bond. In our study, the fluorine substitution for the –OH group caused the shrinkage of the crystal lattice. It could be inferred that the distance of Eu-O bond was decreased correspondingly, which was beneficial for the energy transfer of CTB. Accordingly, the fluorine substitution for the –OH group promoted the process of the energy level transition of Eu^{3+} ions as well as the luminescence.

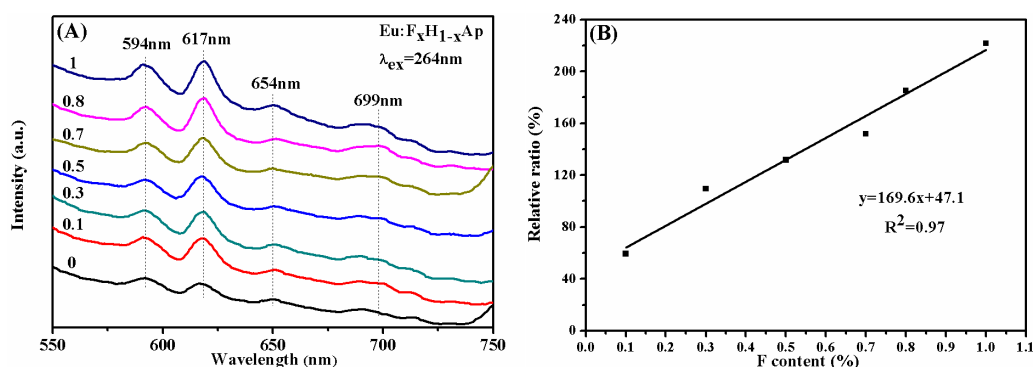


Figure 8. (A) Luminescence spectra of $\text{Eu:F}_x\text{H}_{1-x}\text{Ap}$ ($x = 0, 0.1, 0.3, 0.5, 0.7, 0.8, 1.0$) excitation at 264 nm. (B) The relative ratio with a different fluorine ratio.

4. Conclusions

The $\text{Eu:F}_x\text{H}_{1-x}\text{Ap}$ nanoparticles were synthesized by the hydrothermal method with a different fluorine substitution ratio. With the increase of the fluorine substitution ratio, the luminescence property of $\text{Eu:F}_x\text{H}_{1-x}\text{Ap}$ could be enhanced. The absorption peak intensity of the hydroxyl group gradually decreased with the increase of the fluorine substitution ratio, which indicates that the hydroxyl group was successfully substituted by fluorine ions. The crystal structure of the $\text{Eu:F}_x\text{H}_{1-x}\text{Ap}$ was still composed of a single crystal phase where the crystallinity degree was better than HAp while x was greater than 0.5. When x was increased to 1, the crystallinity degree of $\text{Eu:F}_x\text{H}_{1-x}\text{Ap}$ was the largest, and the maximum was 55.56%. The morphology of $\text{Eu:F}_x\text{H}_{1-x}\text{Ap}$ was mainly a rod-like structure and the length tended to decrease with the increase of the fluorine substitution ratio. The fluorine affected the symmetry of the structure and, thus, changed the surrounding environment in which Eu^{3+} ions are located. Furthermore, regarding the fluorine substitution for the $-\text{OH}$ group, the quenching effect caused by the $-\text{OH}$ group was reduced. In addition, the fluorine ions could produce lower vibration energy and promote luminescence conversion. The fluorine could promote luminescence conversion and luminescence of Eu^{3+} ions would gradually improve with the increase of the fluorine substitution for the $-\text{OH}$ group. There was almost a linear increase when the fluorine substitution ratio increased.

Author Contributions: Conceptualization, Y.H. and X.Z. Methodology, X.Z. and Q.X. Validation, X.Z. and L.L. Investigation, X.Z. and Q.X. Writing-original draft, X.Z. Writing-review and editing, Y.H. All authors have read and agree to the published version of the manuscript.

Funding: The National Key Research and Development Program of China (2016YFB1101302), the National Natural Science Foundation of China (51672206), the Science and Technology Partnership Program, Ministry of Science and Technology of China (KY201602002).

Conflicts of Interest: The authors declare that they have no known competing financial interests.

Appendix A

Table A1. Structural parameters and degree of crystallinity of the $\text{Eu:F}_x\text{H}_{1-x}\text{Ap}$.

Samples ($\text{Eu:F}_x\text{H}_{1-x}\text{Ap}$, x)	$D_{(002)}$ (nm)	$V \times 10^3$ (nm^3)	X_c (%)
0	39.4	529.0	38.73%
0.1	39.8	528.6	35.46%
0.3	40.6	528.0	28.87%
0.5	35.7	527.9	20.87%
0.7	36.5	523.7	21.49%
0.8	32.8	522.2	43.11%
1	33.7	522.5	55.56%

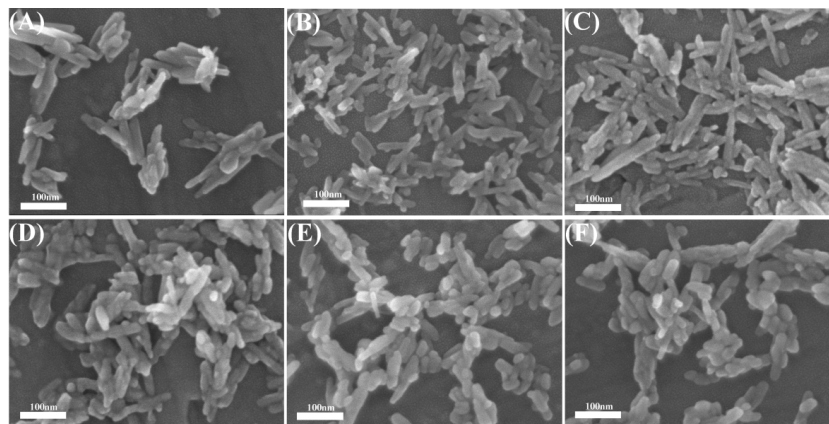


Figure A1. SEM images of the $\text{Eu:F}_x\text{H}_{1-x}\text{Ap}$ with a different fluorine substitution ratio. (A): 0, (B): 0.3, (C): 0.5, (D): 0.7, (E): 0.8, (F): 1.

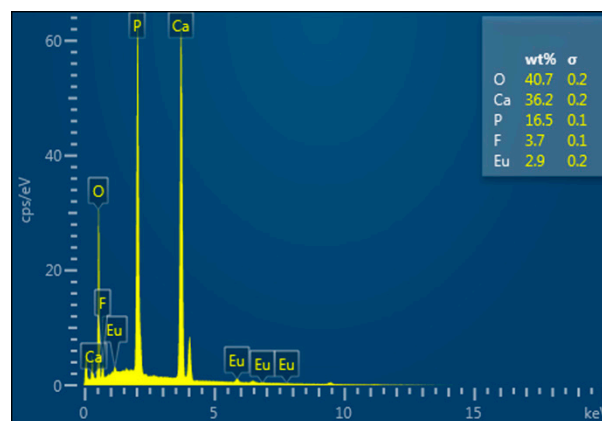


Figure A2. EDS result of Eu:FAp powders prepared by the hydrothermal method.

Table A2. Calculated elemental molar ratios of Eu:FAp .

Molar Ratio	Calculated Value	Observed Value
$\text{Eu}/(\text{Ca} + \text{Eu})$	0.02	0.02 ± 0.01
$(\text{Ca} + \text{Eu})/\text{P}$	1.67	1.69 ± 0.05
$\text{F}/(\text{Ca} + \text{Eu})$	0.2	0.24 ± 0.04

Table A3. Particle sizes of the $\text{Eu:F}_x\text{H}_{1-x}\text{Ap}$ with different fluorine substitution ratio.

Samples ($\text{Eu:F}_x\text{H}_{1-x}\text{Ap}$, x)	Length (nm)	Diameter (nm)	Aspect Ratio (%)
0	77.70 ± 2.88	15.43 ± 0.26	5.04
0.3	54.37 ± 1.78	14.09 ± 0.30	3.86
0.5	47.19 ± 2.55	14.31 ± 0.15	3.30
1	43.36 ± 2.02	14.07 ± 0.49	3.08

References

1. Tesch, A.; Wenisch, C.; Herrmann, K.H.; Reichenbach, J.R.; Warncke, P.; Fischer, D.; Müller, F.A. Luminomagnetic Eu^{3+} - and Dy^{3+} -doped hydroxyapatite for multimodal imaging. *Mater. Sci. Eng. C* **2017**, *81*, 422–431. [[CrossRef](#)] [[PubMed](#)]
2. Niu, N.; Wang, D.; Huang, S.; Li, C.; He, F.; Gai, S.; Li, X.; Yang, P. Controlled synthesis of luminescent F-substituted strontium hydroxyapatite with hierarchical structures for drug delivery. *CrystEngComm* **2012**, *14*, 1744–1752. [[CrossRef](#)]

3. Han, Y.; Wang, X.; Dai, H.; Li, S. Synthesis and luminescence of Eu³⁺ doped hydroxyapatite nanocrystallines: Effects of calcinations and Eu³⁺ content. *J. Lumin.* **2013**, *135*, 281–287. [[CrossRef](#)]
4. Escudero, A.; Calvo, M.E.; Rivera Fernández, S.; de la Fuente, J.M.; Ocaña, M. Microwave Assisted Synthesis of Biocompatible Europium Doped Calcium Hydroxyapatite and Fluoroapatite Luminescent Nanospindles Functionalized with Poly(acrylic acid). *Langmuir* **2013**, *29*, 1985–1994. [[CrossRef](#)]
5. Hui, J.; Zhang, X.; Zhang, Z.; Wang, S.; Tao, L.; Wei, Y.; Wang, X. Fluoridated HAp:Ln³⁺ (Ln = Eu or Tb) nanoparticles for cell imaging. *Nanoscale* **2012**, *4*, 6967–6970. [[CrossRef](#)]
6. Ma, B.; Zhang, S.; Qiu, J.; Li, J.; Sang, Y.; Xia, H.; Jiang, H.; Claverie, J.; Liu, H. Eu/Tb codoped spindle-shaped fluorinated hydroxyapatite nanoparticles for dual-color cell imaging. *Nanoscale* **2016**, *8*, 11580–11587. [[CrossRef](#)]
7. Jiao, L.; Xin, W.; Xi, Y.; Limin, Z.; Zhongxing, Z.; Huijuan, Z.; Feng, G. Towards pH-sensitive imaging of small animals with photon-counting difference diffuse fluorescence tomography. *J. Biomed. Opt.* **2012**, *17*, 096011.
8. Rao, J.; Dragulescu Andrasi, A.; Yao, H. Fluorescence imaging in vivo: Recent advances. *Curr. Opin. Biotechnol.* **2007**, *18*, 17–25.
9. Sobierajska, P.; Wiglusz, R.J. Influence of the grain sizes on Stokes and anti-Stokes fluorescence in the Yb³⁺ and Tb³⁺ ions co-doped nanocrystalline fluorapatite. *J. Alloys Compd.* **2019**, *785*, 808–818. [[CrossRef](#)]
10. Feng, Z.; Li, Y.; Huang, Y.; Seo, H.J. Luminescence properties of Eu²⁺ and Eu³⁺ doped calcium deficient hydroxyapatite prepared in air. *J. Alloys Compd.* **2011**, *509*, 7087–7092. [[CrossRef](#)]
11. Graeve, O.A.; Kanakala, R.; Madadi, A.; Williams, B.C.; Glass, K.C. Luminescence variations in hydroxyapatites doped with Eu and Eu ions. *Biomaterials* **2010**, *31*, 4259–4267. [[CrossRef](#)]
12. Xie, Y.; He, W.; Li, F.; Perera, T.S.; Gan, L.; Han, Y.; Wang, X.; Li, S.; Dai, H. Luminescence Enhanced Eu³⁺/Gd³⁺ Co-Doped Hydroxyapatite Nanocrystals as Imaging Agents In Vitro and In Vivo. *ACS Appl. Mater. Interfaces* **2016**, *8*, 10212–10219. [[CrossRef](#)] [[PubMed](#)]
13. Chen, F.; Huang, P.; Zhu, Y.J.; Wu, J.; Zhang, C.L.; Cui, D.X. The photoluminescence, drug delivery and imaging properties of multifunctional Eu³⁺/Gd³⁺ dual-doped hydroxyapatite nanorods. *Biomaterials* **2011**, *32*, 9031–9039. [[CrossRef](#)] [[PubMed](#)]
14. Zheng, X.; Liu, M.; Hui, J.; Fan, D.; Ma, H.; Zhang, X.; Wang, Y.; Wei, Y. Ln³⁺ doped hydroxyapatite nanocrystals: Controllable synthesis and cell imaging. *Phys. Chem. Chem. Phys.* **2015**, *17*, 20301–20307. [[CrossRef](#)] [[PubMed](#)]
15. Karthi, S.; Kumar, G.A.; Sardar, D.K.; Dannangoda, G.C.; Martirosyan, K.S.; Girija, E.K. Fluorapatite coated iron oxide nanostructure for biomedical applications. *Mater. Chem. Phys.* **2017**, *193*, 356–363. [[CrossRef](#)]
16. Stouwdam, J.W.; Veggel, F.C.J.M.V. Near-Infrared Emission of Redispersible Er³⁺, Nd³⁺, and Ho³⁺ Doped LaF₃ Nanoparticles. *Nano Lett.* **2002**, *2*, 733–737. [[CrossRef](#)]
17. Landi, E.; Tampieri, A.; Celotti, G.; Sprio, S. Densification behaviour and mechanisms of synthetic hydroxyapatites. *J. Eur. Ceram. Soc.* **2000**, *20*, 2377–2387. [[CrossRef](#)]
18. Viorel Marin, R.; Chuen How, N.; Max, W.; Brigitte, T.; Peter, F.; Peter, M.G. Size-controlled hydroxyapatite nanoparticles as self-organized organic-inorganic composite materials. *Adv. Sci. Technol.* **2005**, *53*, 32–37.
19. Binnemans, K. Interpretation of europium(III) spectra. *Coord. Chem. Rev.* **2015**, *295*, 1–45. [[CrossRef](#)]
20. Qin, J.; Zhong, Z.; Ma, J. Biomimetic synthesis of hybrid hydroxyapatite nanoparticles using nanogel template for controlled release of bovine serum albumin. *Mater. Sci. Eng. C Mater. Biol. Appl.* **2016**, *62*, 377–383. [[CrossRef](#)]
21. Doat, A.; Fanjul, M.; Pellé, F.; Hollande, E.; Lebugle, A. Europium doped bioapatite: A new photostable biological probe, internalizable by human cells. *Biomaterials* **2003**, *24*, 3365–3371. [[CrossRef](#)]
22. Hidouri, M.; Albeladi, N. Lanthanum Neodymium Co-Substituted Calcium Fluorobriholites. *J. Mater. Sci. Chem. Eng.* **2018**, *6*, 151–162. [[CrossRef](#)]
23. Biazar, E.; Jahandideh, R.; Majdi, A. Synthesis of fluorapatite– hydroxyapatite nanoparticles and toxicity investigations. *Int. J. Nanomed.* **2011**. [[CrossRef](#)] [[PubMed](#)]
24. Misra, D.N. Adsorption on hydroxyapatite: Role of hydrogen bonding and interphase coupling. *Langmuir* **1988**, *4*, 953–958. [[CrossRef](#)]
25. Misra, D.N. Adsorption from solutions on synthetic hydroxyapatite: Nonaqueous vs. aqueous solvents. *J. Biomed. Mater. Res.* **1999**, *48*, 848–855. [[CrossRef](#)]
26. Santos, C.; Clarke, R.L.; Braden, M.; Guitian, F.; Davy, K.W.M. Water absorption characteristics of dental composites incorporating hydroxyapatite filler. *Biomaterials* **2002**, *23*, 1897–1904. [[CrossRef](#)]

27. Rivas, M.; del Valle, L.J.; Turon, P.; Puiggali, J.; Alemán, C. Influence of the atmosphere conditions in the structure, properties and solubility of fluorine-substituted hydroxyapatites. *Mater. Chem. Phys.* **2019**, *226*, 279–289. [[CrossRef](#)]
28. Xing, Q.; Zhang, X.; Wu, D.; Han, Y.; Nirmali Wickramaratne, M.; Dai, H.; Wang, X. Ultrasound-Assisted Synthesis and Characterization of Heparin-Coated Eu³⁺ Doped Hydroxyapatite Luminescent Nanoparticles. *Colloid Interface Sci. Commun.* **2019**, *29*, 17–25. [[CrossRef](#)]
29. Gaft, M.; Reisfeld, R.; Panczer, G.; Shoval, S.; Champagnon, B.; Boulon, G. Eu³⁺ luminescence in high-symmetry sites of natural apatite. *J. Lumin.* **1997**, *72–74*, 572–574. [[CrossRef](#)]
30. Ternane, R.; Panczer, G.; Cohen Adad, M.T.; Goutaudier, C.; Boulon, G.; Kbir Ariguib, N.; Trabelsi Ayedi, M. Relationships between structural and luminescence properties in Eu³⁺-doped new calcium borohydroxyapatite. *Opt. Mater.* **2001**, *16*, 291–300. [[CrossRef](#)]
31. McGahan, W.A. 6—Materials Characterization. In *Handbook of Magento-Optical Data Recording*; Elsevier: Amsterdam, The Netherlands, 1995; pp. 362–424.
32. KlixbüllJørgensen, C.; Judd, B.R. Hypersensitive pseudoquadrupole transitions in lanthanides. *Mol. Phys.* **1964**, *8*, 281–290.
33. Zhang, X.; Tan, Q.; Hu, S.; Yang, J. Hydrothermal synthesis of ScVO 4: Ln 3+ (Ln = Eu, Dy, Eu/Dy) microcrystals with controllable morphology, energy transfer and multicolor luminescence. *Mater. Chem. Phys.* **2018**, *215*, 259–268. [[CrossRef](#)]



© 2020 by the authors. Licensee MDPI, Basel, Switzerland. This article is an open access article distributed under the terms and conditions of the Creative Commons Attribution (CC BY) license (<http://creativecommons.org/licenses/by/4.0/>).